

Anatomy of October 30, 2020, Samos (Sisam) –Kuşadası earthquake (MW 6.92) and its influence on Aegean earthquake hazard

Fatih BULUT^{1*}, Aslı DOĞRU¹, Cenk YALTIRAK², Sefa YALVAÇ³, Murat ELGE⁴

¹Department of Geodesy, Kandilli Observatory and Earthquake Research Institute, Boğaziçi University, İstanbul, Turkey

²Department of Geology, Faculty of Mines, İstanbul Technical University, İstanbul, Turkey

³Department of Survey Engineering, Faculty of Engineering, Gümüşhane University, Gümüşhane, Turkey

⁴Turkish Office of Navigation, Hydrography and Oceanography, İstanbul, Turkey

Received: 24.02.2021 • Accepted/Published Online: 17.04.2021 • Final Version: 16.07.2021

Abstract: We investigated rupture geometry, size, and slip distribution of October 30, 2020, Samos (Sisam)–Kuşadası earthquake combining seismographs, GPS measurements, and SAR analysis. Right after the earthquake, we measured 13 additional campaign-based GPS sites to intensify the available GPS network consisting of 10 continuous stations. We combined all available seismographs to have the best possible accuracy for mainshock and aftershock hypocenter locations. We compiled all available seismic profiles and integrated them using high-resolution bathymetry to map seismically active faults. The mainshock hypocenter is located at 37.913 ± 0.009 N° and 26.768 ± 0.017 E° and a depth of 12.3 ± 1.7 km. Our fault plane solution shows that the mainshock has almost a pure normal-type mechanism. Based on accurate aftershock locations as well as InSAR results, the mainshock rupture is subsegmented with two north-dipping rupture planes. The rupture probably starts on a low angle plane generating 1.1 m average slip between the depths of 9–14 km. It merges to a steep plane at 9 km depth where it generates 1.2 m average slip extending towards the surface near the shoreline of Samos (Sisam) Island. Total size of the two rupture planes and their average slips determine that the magnitude of the mainshock is (M_w) 6.92 ± 0.02 . The mainshock has substantially increased Coulomb stress on several fault segments near the towns Kuşadası and Söke, which have the potentials to generate strong earthquakes. It also nonnegligibly increased Coulomb stress on several fault segments south of İzmir giving a warning for increased earthquake hazard in this highly inhabited area.

Key words: 2020 Samos (Sisam)–Kuşadası earthquake, earthquake hazard, earthquake source observations, seismicity and tectonics, GPS, InSAR

1. Introduction

A magnitude 6.92 earthquake has shaken the Turkish-Greek border on October 30, 2020. Its hypocenter is located at a 60 km distance to the south from the city center of İzmir, the third-largest city of Turkey, and just 10 km offshore from Samos (Sisam) Island (Figure 1). The earthquake resulted in a total of 115 fatalities, 1034 injuries, and thousands left from their houses.¹ In this highly inhabited region, the strong mainshock has probably redistributed earthquake hazard changing Coulomb stress on nearby seismically active faults.

The region is dominated by an extensional tectonic regime due to the rollback of the subducting African Plate beneath the Aegean Sea (e.g., McClusky et al., 2000; Nyst and Thatcher, 2004). In this tectonic setting, extending and therefore subsiding the floor of the Aegean Sea might

accommodate plenty of normal faults pending at the ready-to-fail stage. Seismic potential in the vicinity of İzmir has been verified by intensified GPS measurements (Aktug and Kılıçoğlu, 2006; Doğru et al., 2014; Sozbilir et al., 2020; Eyübagil et al., 2021). In this context, the region accommodates M 6+ earthquakes as documented by the historical and the instrumental period records (Stiros et al., 2000; Eyidoğan, 2020).

Investigating Coulomb stress changes following such strong earthquakes is therefore crucial as they might suddenly load years of strain storage in a few seconds shortening the interseismic stages of adjacent fault segments. To investigate the Coulomb stress change generated by the M_w 6.92 mainshock on nearby faults, its rupture geometry, size, and slip distribution must be identified accurately.

¹ Disaster and Emergency Management Presidency of Turkey (2021). İzmir Seferihisar Depremi – Duyuru 77 [online] (in Turkish). Website <https://www.afad.gov.tr/izmir-seferihisar-depremi-duyuru-77-13112020---1800> [accessed 17 November 2020].

* Correspondence: bulutf@boun.edu.tr

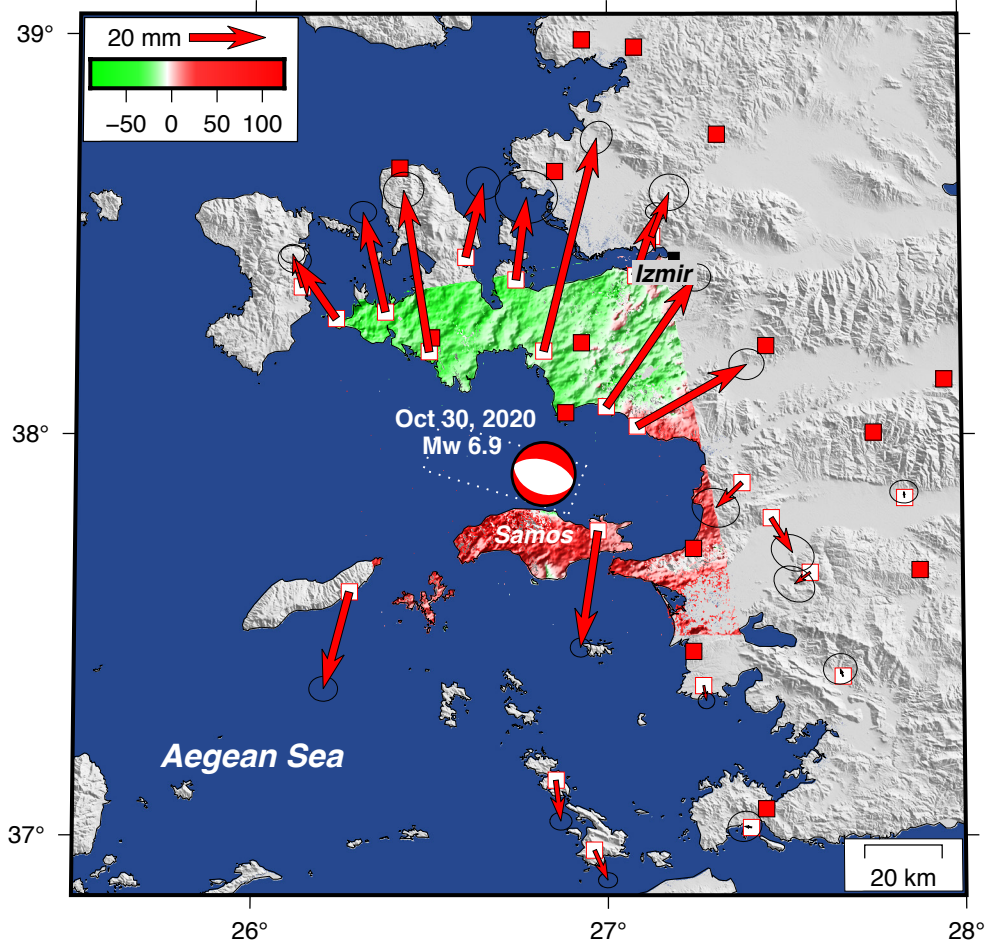


Figure 1. Geodetic data used for characterization of the October 30, 2020, Samos (Sisam)–Kuşadası M_w 6.92 earthquake. Red arrows show GPS-derived horizontal surface displacements. Red and green shadows show SAR-derived surface displacements in LOS. Beach ball shows the location as well as the focal mechanism of the mainshock. The white dashed line shows the rupture plane. Red squares are seismographs that are used for aftershock locations. The inset figure shows the study area on a regional scale.

The slip distribution of a strong earthquake is simulated by back-projecting its coseismic surface displacements onto its rupture plane using elastostatic Green's functions (Okada, 1985). GPS is currently the most accurate technology to measure surface displacements. It provides a millimeter-scale of positioning accuracy for displacements in the order of centimeters, which strong earthquakes are expected to generate in their vicinity (Hager et al., 1991).

In this study, we measured static surface displacements that are generated by the October 30, 2020, Samos (Sisam)–Kuşadası earthquake (M_w 6.92) using GPS and SAR technologies. In addition to continuous GPS stations from Turkish and Greek sides, we performed a GPS campaign to capture near field surface displacements. Location, geometry, and predominant slip direction of the mainshock were firstly investigated using seismographs. The ambiguity between the nodal rupture planes was

resolved using accurate aftershock locations. In a second step, we used surface displacements to improve these source parameters. We further analyzed surface displacements to investigate co-seismic slip distribution on the rupture plane. Compiling active seismic data in the light of high-resolution bathymetry, we mapped seismically active faults in the vicinity of the mainshock. We finally modeled Coulomb stress change on nearby seismically active faults to investigate the influence of the October 30, 2020, Samos (Sisam)–Kuşadası earthquake (M_w 6.92) on the earthquake hazard of this highly inhabited region.

2. Location and focal mechanism of the mainshock

We carefully investigated the hypocenter and focal mechanism of the mainshock combining 115 regional seismographs that are operated by Boğaziçi University, Kandilli Observatory and Earthquake Research Institute

(KOERI), Disaster and Emergency Management Presidency (AFAD), National Observatory of Athens (NOA), and Aristotle University of Thessaloniki (AUTH). Azimuthal coverage of seismographs surrounding the mainshock hypocenter is better than 68°.

The hypocenter location of the mainshock was determined using hand-picked P-wave first arrival times. For the travel time modeling, we used a reference 1-D velocity model, which has been previously optimized by Bulut et al. (2009). The least-square inversion was performed by the HYPOCENTER earthquake location program (Lienert and Havskov, 1995). Initial polarities of P-wave first motions were used to optimize the best-fitting strike, dip, and rake angles of the focal mechanism. We used the FOCMEC fault plane solution program for grid search (Snoke, 2003).

The mainshock hypocenter (nucleation point) is located at 37.913N° and 26.768E° and a depth of 12.3 km. Hypocenter location uncertainty is 1.3 km on the horizontal axis and 1.7 km at depth. Mainshock hypocenter has been located using P-wave arrivals from 33 seismographs. Fault plane solution shows almost a pure normal-type focal mechanism with a minor lateral component. The strike of the rupture plane is 108° clockwise located from the geographical north. However, fault plane solutions cannot discriminate between the two nodal planes to determine whether the rupture plane dips to the north or the south. We resolve this ambiguity using accurate aftershock locations.

3. Aftershock locations

We refined hypocenter locations of aftershocks to characterize the geometry of the fault planes accommodating the postearthquake activity. For aftershock locations, we used a total of 24 near-field seismographs that are operated by KOERI and AFAD (Figure 1). The hypocenter location method is described above in Section 2. For fault plane characterization, we consider only well-located aftershocks, of which the location uncertainty is less than 1.5 km, both in horizontal and vertical axes.

For the first six days following the mainshock, we obtained 816 well-located aftershocks. Figure 2 shows locations of these aftershocks on map view as well as along north-south oriented depth profiles. In the west of the mainshock hypocenter, aftershock activity was prominently low. Aftershocks occurred mostly in the east of the mainshock hypocenter, to the north of the Samos (Sisam) Island right beyond its northern shoreline (Figure 2). There, the aftershocks indicate a north-dipping low angle plane between the depths of 8–14 km (Figure 2). The inclination is in good agreement with the north-dipping

nodal plane of the mainshock fault plane solution (Figures 1 and 2). This resolves the nodal plane ambiguity and identifies that the rupture plane of the mainshock dips to the north. The final location and fault plane solution for the mainshock are given in Table 1.

4. GPS-derived surface displacements

We intensified near-field observations with a GPS campaign that we performed right after the 2020 Samos (Sisam)–Kuşadası earthquake measuring 13 additional stations. We combined this data with 10 regional GPS stations, which are continuously operated by The General Directorate of Land Registry and Cadastre, and The General Directorate of Mapping on the Turkish side, and Treecomp Company on the Greek side. We totally used 23 GPS stations. From continuous stations, GPS data span five days before and three days after the mainshock. For campaign-based stations, we used at least 6-h of sessions measured in 2018 and 2020, before and after the earthquake, respectively. All GPS data were sampled at 30 s. The cutoff for elevation angle was fixed at 10 degrees.

GPS data were analyzed on daily basis using GAMIT/GLOBK GPS processing software (Herring et al., 2010). Stabilization was performed in ITRF2014 reference frame with fourteen IGS stations. IGS final orbits were obtained from Scripps Orbit and Permanent Array Center.² Bulletin B earth orientation parameters were obtained from the United States Naval Observatory.³ An elevation-dependent model was applied for the receiver antenna phase center calibrations. Tropospheric delay governed by temperature, pressure, and humidity was minimized using GMF (global mapping function) model in 2-h intervals (Boehm et al., 2006). The FES2004 ocean tide loading (OTL) global grid was used for ocean tide modeling (Lyard et al., 2006). IERS2003 was used for the earth tide and pole tide model (McCarthy and Petit, 2004). Loosely constrained solutions were estimated in ITRF2014 by GAMIT and GLRED was used to estimate north, east and up components at each epoch (Herring et al., 2010).

Coseismic displacements we observed range between 3.0 and 115.2 mm within a distance range of 24.6 to 131.4 km from the mainshock hypocenter (Table 2). Positioning errors range between 2 and 6 mm for all epochs. GPS measurements show that the surface displacements occur mainly in the north-south axis with a minor east-west component. They predominantly move to the north in the northern quadrants, and to the south in the southern quadrants (Figures 1 and 3). North-south displacements reach up to 111.8 mm while east-west displacements remain below 57.4 mm. First-order evaluation of this overall pattern suggests a north-south extension on an east-

² Scripps Orbit and Permanent Array Center (SOPAC) (2021). IGS final orbits [online]. Website <http://sopac-csrc.ucsd.edu> [accessed 00 Month Year].

³ United States Naval Observatory (USNO) (2021). Earth orientation parameters [online]. Website <http://usno.navy.mil> [accessed 00 Month Year].

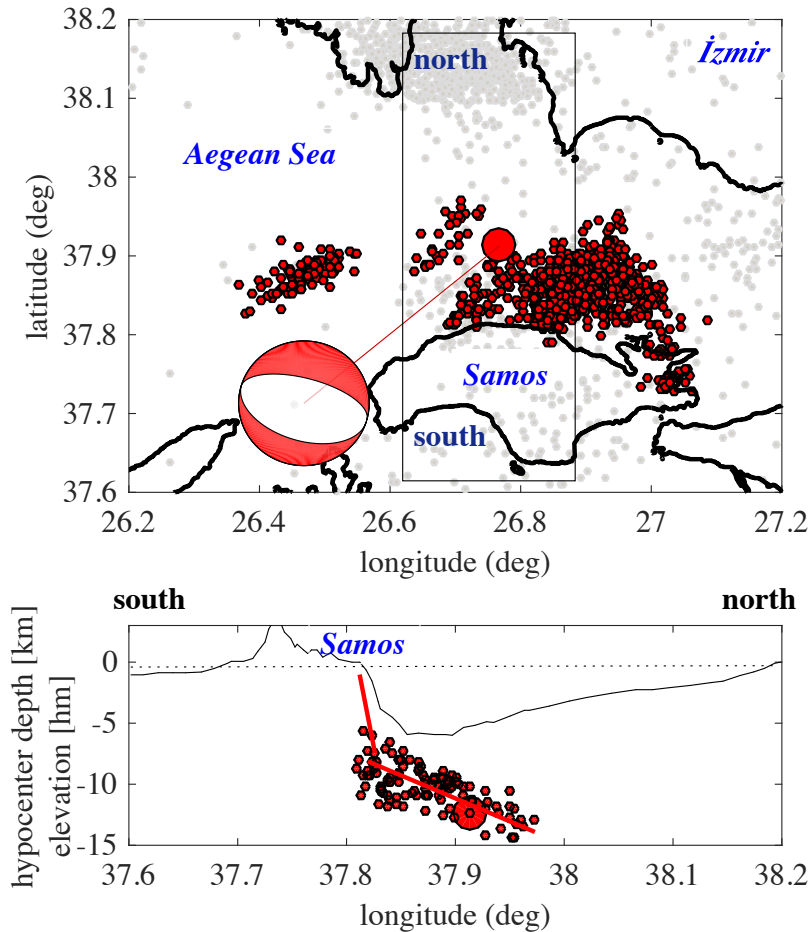


Figure 2. Gray dots show the locations of earthquakes reported by KOERI for the time period of 2005–2020 before the Oct 30, 2020 Mw 6.92 mainshock. Red dots show aftershock locations. The large red dot shows the mainshock location. The upper panel is the map view of the 2020 Samos (Sisam)–Kuşadası aftershock locations. The rectangle frames the aftershock epicenters that are selected for the cross sectional view in the lower panel. Beach ball shows the focal mechanism of the mainshock. The lower panel is a south-north oriented depth sectional view of the aftershock hypocenters in the vicinity of the mainshock hypocenter. The red line shows the segmentation of the rupture plane that we used for slip inversion.

west trending fault plane. This verifies the seismograph-derived fault plane solution of the mainshock.

5. SAR-derived surface displacements

We used the Sentinel S1A Synthetic Aperture Radar (SAR) image data framing the rupture zone of the 30 October 2020 earthquake. The SAR images correspond to the only ascending orbit direction on track 160 with master 201018 and slave 201030. The conventional two-pass differential interferometry approach was adopted to produce interferograms from the SLC products using the GMT5SAR software developed at UCSD (Sandwell et al., 2016). SAR analysis includes three basic steps: (1) geometric alignment based on precise orbits (Sansosti et al., 2006), (2) deramping of SLC data before interpolation (Miranda, 2014), and (3) overall correction of misregistration errors based on

enhanced spectral diversity. The topographic phase was removed using a 1-arc-second Shuttle Radar Topography Mission Digital Elevation Model (SRTM DEM) (Farr et al., 2007). The interferograms were smoothed with a power spectrum filter (Goldstein and Werner, 1998), and then to obtain the displacements unwrapping process was carried out in SNAPHU and the results obtained were geocoded (Chen, 2001).

Figure 1 shows results from the analysis of SAR data, measured changes in satellite-ground distances at 30.67° of line-of-sight (LOS). SAR results clearly show that Samos (Sisam) Island, which is located to the south of the rupture plane, is exposed to uplift in response to the mainshock. In contrast, the İzmir region, to the north of the focal area, accommodates subsidence. This pattern mechanically verifies that the rupture plane dips to the north.

Table 1. Location and source parameters of the mainshock.

Source	Latitude [°]	Longitude [°]	Depth [km]	Mw	Strike [°]	Dip [°]	Rake [°]
This study	37.913 ± 0.009	26.768 ± 0.017	12.3 ± 1.7	6.92 ± 0.02	108.4 ± 2.8	33.0 ± 2.3	-88.3 ± 3.4
KOERI	37.902	26.794	12.0	6.9	97	34	-85
AFAD	37.888	26.777	11.1	6.6	95	43	-87
NOA	37.900	26.806	12.0	6.9	76	43	-120
USGS	37.918	26.790	21.0	7.0	93	60	-91
GFZ	37.900	26.820	10.0	7.0	97	41	-85
INGV	37.840	26.810	10.6	7.0	82	53	-107

Table 2. GPS-derived surface displacements generated by the Oct 30, 2020 Samos (Sisam) –Kuşadası earthquake (M_w 6.92).

Location [°]		Displacement [mm]		Uncertainty [mm]		Distance to epicenter [km]	Total displacement [mm]
Longitude	Latitude	East	North	East	North		
26.82	38.21	27.7	111.8	3.5	3.4	32.8	115.2
26.50	38.20	-13.5	84.8	3.9	4.3	39.7	85.9
27.00	38.07	46.9	67.8	2.9	3.3	25.9	82.4
27.08	38.02	57.4	32.4	3.3	3.8	29.3	65.9
26.97	37.76	-9.2	-61.0	2.0	2.2	24.6	61.7
26.37	38.30	-11.8	52.3	2.3	2.9	54.9	53.6
26.27	37.60	-13.4	-50.7	2.6	3.1	54.2	52.4
26.74	38.38	5.5	43.5	5.7	6.6	52.3	43.8
26.60	38.44	9.2	38.8	3.4	3.6	60.3	39.9
26.23	38.29	-21.9	31.2	2.9	3.5	61.6	38.1
27.08	38.40	11.0	33.6	1.9	2.3	59.8	35.4
27.13	38.49	9.3	23.3	3.9	4.2	71.1	25.1
26.85	37.14	2.6	-21.4	1.9	2.4	86.6	21.6
27.46	37.79	11.2	-18.3	3.9	4.6	60.5	21.5
27.38	37.88	-13.7	-13.2	4.2	5.1	52.1	19.0
26.14	38.37	-5.0	17.5	2.0	2.6	73.6	18.2
26.96	36.96	7.0	-15.7	1.6	2.0	106.8	17.2
27.57	37.65	-8.3	-6.1	3.9	4.4	74.0	10.3
27.27	37.37	1.4	-8.0	1.7	1.8	73.6	8.1
28.12	38.48	5.4	1.4	2.0	2.5	131.4	5.6
27.66	37.40	-1.4	3.9	3.3	3.6	95.2	4.1
27.40	37.02	-3.5	0.5	3.2	3.6	112.9	3.5
27.84	37.84	-0.2	3.0	2.4	3.0	91.2	3.0

6. Rupture model

We analyzed slip distribution of the mainshock back-projecting GPS and SAR-derived surface displacements onto these two rupture planes using elastostatic Green's functions (Wang et al., 2009). The bootstrap analysis shows that uncertainties of observed coseismic slips are at a level

of few centimeters along the entire rupture plane (Figure 3). Slip inversion achieved a 93% correlation between the observed and the modeled surface displacements. We used the steepest descent/gradient inversion method to investigate coseismic slip distribution along the rupture plane (Wang et al., 2009). The method employs Okada's

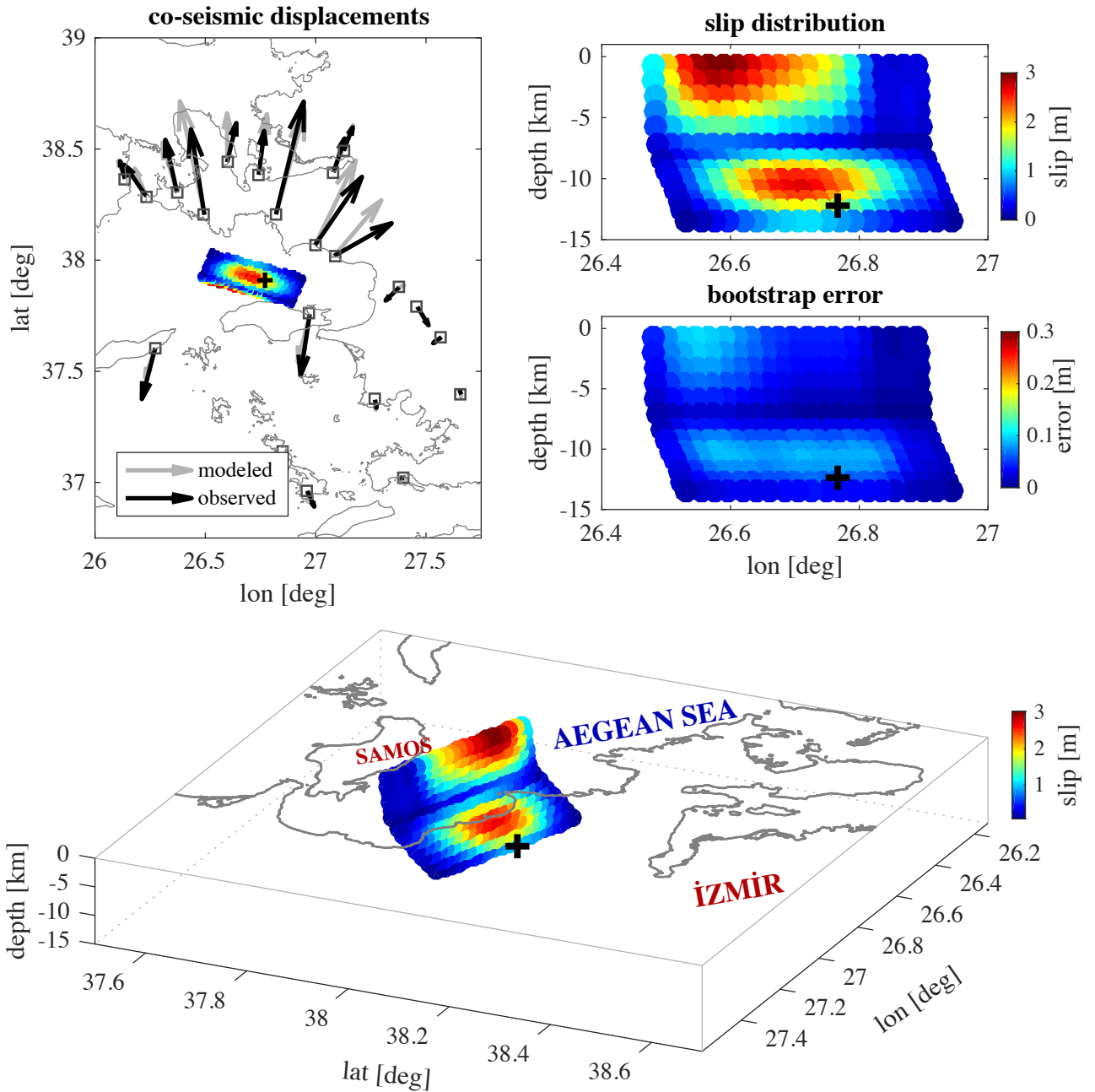


Figure 3. The left panel is a comparison between observed and modeled displacements. Black dots show the modeled rupture plane in map view. The right upper panel is the coseismic slip generated by the October 30, 2020, Samos (Sisam)–Kuşadası M_w 6.92 earthquake obtained from slip inversion of GPS-derived surface displacements. Right lower panel is the bootstrap error distribution for the slip model. Black plus indicates the hypocenter (nucleation point) of the mainshock. The bottom panel shows slip distribution of the mainshock in 3D view.

semi-infinite space model simulating elastic Green's functions to project the dislocations on the fault plane onto the surface (Okada, 1985). In the first step, we used only one patch to investigate strike-slip and dip-slip components of the fault slip which correspond to the rake and magnitude of the slip on the rupture plane. In a second step, we

subdivided the rupture plane into 2×2 km grid patches to investigate the distribution of the fault slip. Distributed slip inversion is an underdetermined problem as the number of slip deficit patches is much larger than the number of coseismic GPS offsets. The employed methodology both regularizes the underdetermined problem and

incorporates additional physical constraints (Bouchon, 1997; Wang et al., 2009). We additionally implemented a bootstrap scheme for a parameterization-independent error assessment and optimized the smoothing factor of the Laplacian operator comparing smoothing factors and the resulting sum of squared errors.

Integrating mainshock location, its focal mechanism, aftershock locations, SAR-based displacements lead us to the conclusion that the rupture has two north-dipping planes with different inclinations. The lower rupture plane extends between the depths of 9–14 km covering also the mainshock hypocenter. Combining the fault plane solution of the mainshock as well as the north-south profile view of the aftershock locations, the lower rupture plane must dip to the north at $\sim 30^\circ$. SAR results indicate that the upper rupture plane must surface close to the northern shoreline of the Samos (Sisam) Island to the north. The upper rupture plane must be therefore inclined at $\sim 75^\circ$ between the depths of 0–9 km.

The lower rupture plane is 40 km long and 11 km wide. Its maximum coseismic slip reaches up to 2.7 m while the average slip remains at 1.1 m. There, a high slip patch is localized above the mainshock hypocenter to the west. The upper rupture plane is 40 km long and 9.5 km wide. Its maximum coseismic slip reaches up to 3.0 m while the average slip remains at 1.2 m. There, a high slip patch is localized to the further west from the mainshock hypocenter. The overall pattern shows that rupture initiated in the lowermost edge of the lower plane and propagated both upward and westward leaving two localized coseismic slip patches on each rupture plane (Figure 3).

The total size of these two rupture planes and their corresponding average slips determines that the magnitude (M_w) of the 2020 Samos (Sisam)–Kuşadası earthquake is 6.92 (Kanamori, 1983). Varying rigidity in a range of 30–34 GPa or the average slips within bootstrap uncertainty margins of few centimeters determines that the uncertainty of magnitude estimation ± 0.02 .

7. Fault map

Investigating the influence of the 2020 Samos (Sisam)–Kuşadası earthquake on earthquake hazard requires a detailed fault map in the vicinity of the mainshock. In this context, we compiled all available controlled-seismic profiles imaging depth view of the seismically active faults. We reinterpreted fault maps based on seismic sections published previously (Lykousis et al., 1995; Saatçiler et al., 1999; Ocakoğlu et al., 2004; Kuşçu et al., 2010; Gürçay, 2014). The faults are marked with dots along the seismic lines where they are captured. A new fault map was generated with these markers that coincide with the fault traces in the bathymetry. Thus, fault maps were corrected using morphological traces in high-resolution bathymetry.

We focused on the region remaining between the southern shoreline of İzmir and northern shorelines of Ikaria and Samos (Sisam) Islands, basically through the Gulf of Kuşadası, the Gulf of Sığacık and the Ahikerya Basin. Outside of this region, active faults were obtained from the GEM database for stress change analysis (Styron and Pagani, 2020).

We combined two different types of seafloor bathymetry to verify the surface projection of major structures, e.g., basins, and faults. Bathymetry data firstly were digitized using sonar-based sea navigation maps where resolutions are 5 m, 10 m and 20 m for the depth ranges of 0–200 m, 200–600 m, and 600–1100 m, respectively. The resulted bathymetry was then combined with high-resolution multibeam echosounder and single beam echosounder data, which have been provided by Turkish Office of Navigation, Hydrography and Oceanography to get more accurate seabed morphology. Locations of combined seismic profiles, digitized bathymetry data, and the final fault map are given in Figure 4.

Morphology of the study area is characterized by WNW-ESE and WSW-ENE striking normal faults dipping both to the south and the north. They are intersected by NNE-SSW striking dextral faults. This overall pattern indicates that the study area extends in N-S orientation. The extension is older in the west compared to the east of the study area, as verified by asymmetric and deep Ahikerya Basin (Figure 4).

8. Coulomb stress change

Based on the rupture model, we modeled Coulomb stress change on nearby seismically active faults to quantify the influence of the 2020 Samos (Sisam)–Kuşadası earthquake on future earthquake hazard. Stress change modeling was performed by using the Coulomb software, which has been developed by Toda et al. (2011). Coulomb stress is a resultant of shear and normal components of the stress changes on specified target fault planes (King et al., 1994). The static stress changes in shear and normal stresses due to a source earthquake strongly depend on the location, geometry, and slip magnitude of the source earthquake. While other yield criteria are also possible, the most common one is the Coulomb criterion. In this respect, the accuracy of the Coulomb stress changes highly relies on the source slip model. Using the highly accurate slip model as computed in the previous step, Coulomb stress changes were computed at neighboring faults. We assumed that the frictional coefficient is 0.8 based on the measurements compiled by Townend and Zoback (2000). Kinematic characters of the receiver faults are defined as provided in Figure 4. As shown in Figure 5, we classified the faults into three groups based on the Coulomb stress changes they are exposed to.

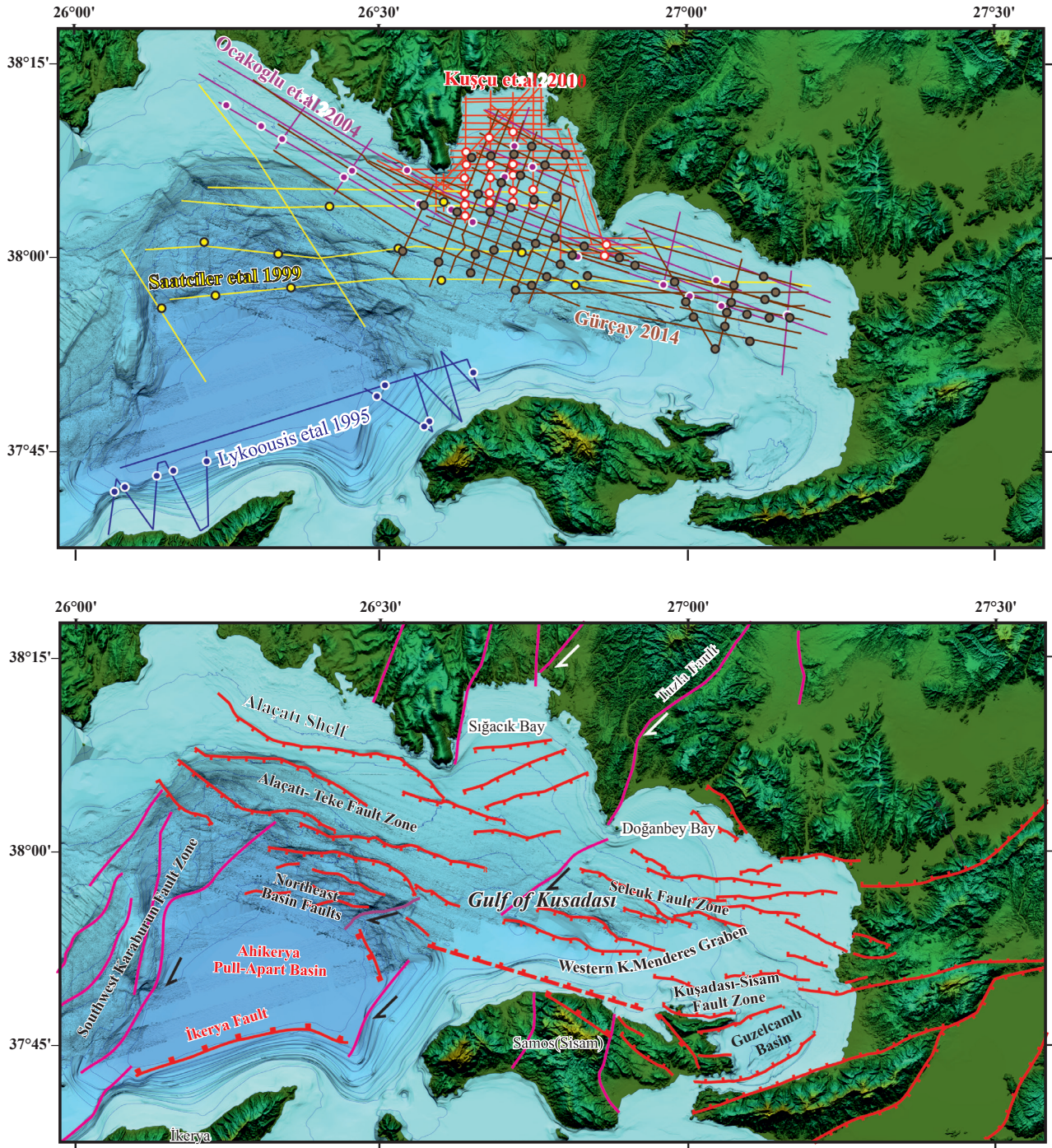


Figure 4. Upper map shows bathymetry data and locations of combined seismic profiles. Lower map shows the fault map generated by combining active seismic profiles and bathymetry. Transparent red lines show verified normal fault segments, and purple ones show strike slip faults. The dashed line represents the surface projection of the rupture.

The first group of faults host Coulomb stress increases below 0.1 bar, a previously observed triggering threshold according to Reasenberg and Simpson (1992). There are 13 fault segments in this group remaining below the triggering threshold (shown by green lines in Figure 5).

The second group of faults hosts nonnegligible Coulomb stress increases between 0.1 and 1.0 bar. There are 20 fault segments in this group (shown by orange lines in Figure 5). Their lengths range from 21 to 54 km and therefore have the potentials to generate M 6+ earthquakes, e.g., the

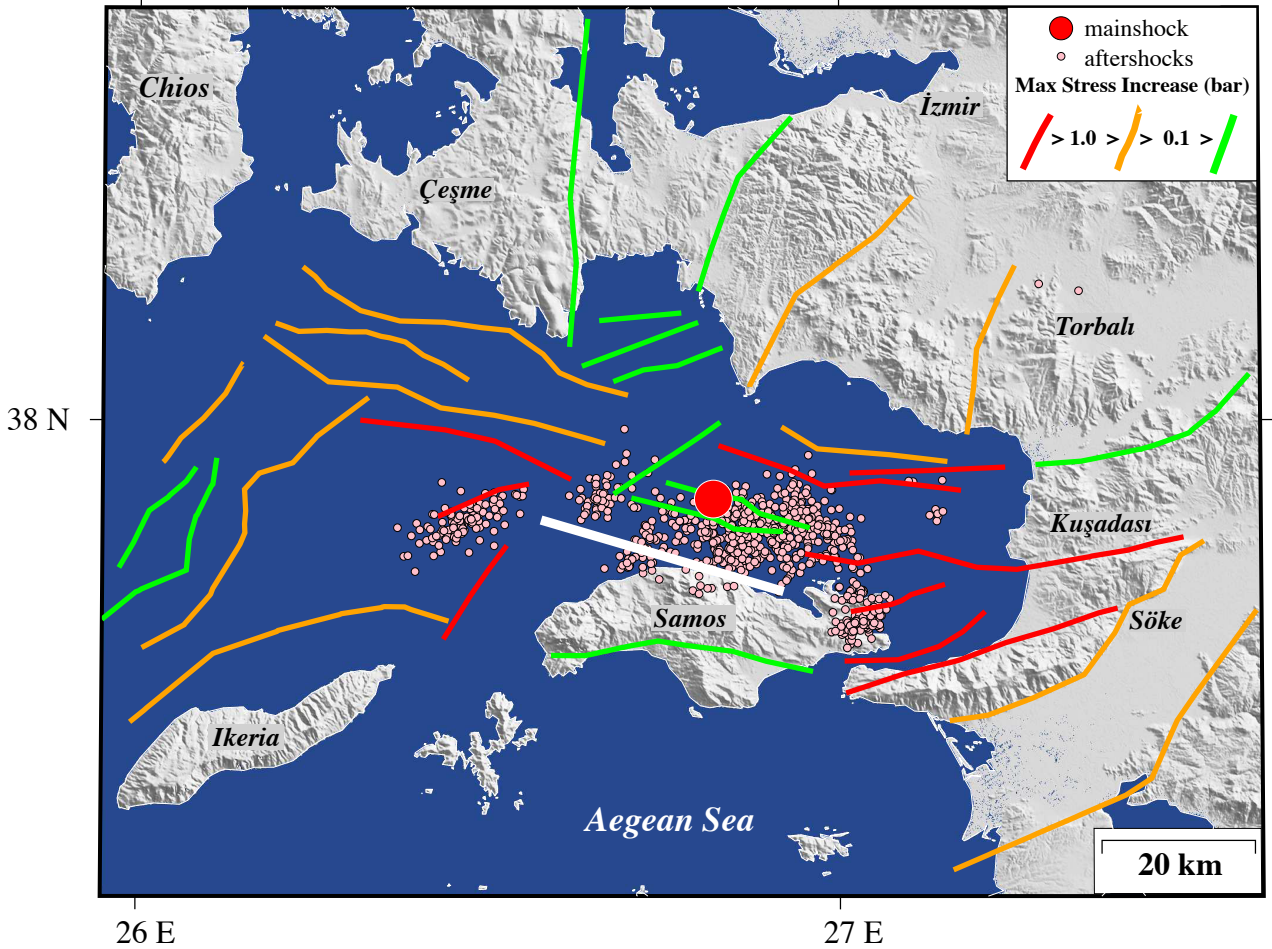


Figure 5. Coulomb stress change on nearby faults following the October 30, 2020, Samos (Sisam)–Kuşadası M_w 6.92 earthquake. The white line shows the surface projection of the mainshock rupture. Red dot shows the mainshock epicenter. Pink dots show aftershock epicenters.

Tuzla Fault south of İzmir and Alaçatı–Teke fault south of Çeşme (Fault locations are available in Figure 4).

The third group of faults hosts substantial Coulomb stress increases above 1.0 bar (shown by red lines in Figure 5). There are 10 fault segments in this group. Their lengths range from 12 to 53 km. The two of these fault segments have already accommodated prominently high aftershock activity (Figure 5). Five of them are longer than 25 km and have the potentials to generate M 6+ earthquakes. Three of these relatively long segments are located very close to highly populated towns, namely Kuşadası and Söke, and give a warning for increased earthquake hazard for the region where more than 200.000 people currently reside.

8. Discussion

Our fault plane solution for the mainshock is based on polarities of P-wave first motion, which is rather sensitive to the initial rupture process. The mechanism is almost a

pure normal-type with a negligible obliquity. This overall pattern is also confirmed by the other studies (Kalogeras et al., 2020; Papadimitriou et al., 2020; Akinci et al., 2021). The double-couple assumption results in two nodal planes; one steeply dips to the south and the other one gently dips to the north. Of these two nodal planes, which corresponds to the initial rupture plane is ambiguous. At this point, we employed accurate aftershock locations in the vicinity of the mainshock hypocenter (Figure 2).

The north-south depth profile of the aftershocks indicates a north-dipping pattern at 30° leading us to the conclusion that the initial rupture occurs on a low angle north dipping fault plane. This gentle plane geometrically should surface at the southern shoreline of Samos (Sisam) Island. However, our SAR analysis, as well as GPS-derived vertical displacements by Ganas et al. (2020), indicates that the Samos (Sisam) Island substantially elevated as a response to the mainshock. In this context, the rupture surfaces in the north of Samos (Sisam) Island.

The mainshock nucleation point (hypocenter) is close to the lower edge of the rupture plane at 12.3 ± 1.7 km depth. It is located on the lower rupture plane, which gently inclined to the north as confirmed by the depth view of aftershock hypocenters. This suggests that the rupture might have initiated close to the lower edge of the rupture plane, and propagated upward along a north-dipping plane at 30° between the depths of 9–14 km. The rupture then merged to a north-dipping steep plane, at 75° between the depths of 0–9 km, based on the coseismic elevation of Samos (Sisam) Island. The rapid slip model also indicates segmentation of the rupture although it assumes a single plane and does not consider double inclination as the seismological findings described above were not yet known therein (USGS finite rupture model⁴).

9. Conclusion

The mainshock is nucleated at 37.913 ± 0.009 N° and 26.768 ± 0.017 E° and a depth of 12.3 ± 1.7 km. Its focal mechanism is almost a pure normal-type with a negligible obliquity. The rupture has occurred on two different planes: In the lower plane, it generated a 1.1 m average slip along a low angle plane, which is $\sim 30^\circ$ dipping to the north between the depths of 9–14 km. The rupture merged to a relatively steep plane, which is $\sim 75^\circ$ dipping to the north between the depths of 0–9 km, generating 1.2 m average

⁴ USGS (2021). USGS Finite Rupture Model [online]. Website <https://earthquake.usgs.gov/earthquakes/eventpage/us7000c7y0/finite-fault> [accessed 08 December 2020].

References

- Akinci A, Cheloni D, Dindar AA (2021). The 30 October 2020, M7.0 Samos Island (Eastern Aegean Sea) Earthquake: effects of source rupture, path and local-site conditions on the observed and simulated ground motions. *Bulletin of Earthquake Engineering* 1-27. doi: 10.21203/rs.3.rs-215817/v1
- Aktuğ B, Kılıçoğlu A (2006). Recent crustal deformation of Izmir, Western Anatolia and surrounding regions as deduced from repeated GPS measurements and strain field. *Journal of Geodynamics* 41 (5): 471-484.
- Bouchon M (1997). The state of stress on some faults of the San Andreas system as inferred from near-field strong motion data. *Journal of Geophysical Research: Solid Earth* 102 (B6): 11731-11744.
- Bulut F, Bohnhoff M, Ellsworth WL, Aktar M, Dresen G (2009). Microseismicity at the North Anatolian fault in the Sea of Marmara offshore Istanbul, NW Turkey. *Journal of Geophysical Research: Solid Earth*, 114 (B9).
- Chen CW (2001). Statistical-cost network-flow approaches to two-dimensional phase unwrapping for radar interferometry. PhD, Stanford University, Stanford, CA, USA.
- Demir A, Çiftçiöğlü A.Ö, Sınır B.G, Başarı E, Doğan E, Nohutcu H. et al. (2020). İzmir (Seferihisar-Sisam) Depreminin Sismik Özellikleri ve Meydana Gelen Yapısal Hasarlara Ait İnceleme ve Değerlendirme Raporu. MCBU Civil Engineering Reports. MCBUCIVILENG.R-2020.2. Manisa Celal Bayar Üniversitesi, Manisa, Turkey: (in Turkish with an abstract in English). 118 s.
- Dogru A, Gorgun E, Ozener H, Aktuğ B (2014). Geodetic and seismological investigation of crustal deformation near Izmir (Western Anatolia). *Journal of Asian Earth Sciences* 82: 21-31.
- Eyidoğan H (2020). Report on the seismological characteristics and effects of the 30 October 2020 Samos-Kuşadası Bay earthquake (Mw7. 0) in the western Aegean Sea. ResearchGate Preprint.
- Eyübagil EE, Solak Hİ, Kavak US, Tiryakiöğlü İ, Sözbilir H et al. (2021) Present-day strike-slip deformation within the southern part of İzmir Balıkesir Transfer Zone based on GNSS data and implications for seismic hazard assessment, western Anatolia. *Turkish Journal of Earth Sciences* 30 (2): 143-160. doi: 10.3906/yer2005-26
- Farr TG, Rosen PA, Caro E, Crippen R, Duren R et al. (2007). The shuttle radar topography mission. *Reviews of Geophysics* 45 (2).

slip. Total size of the two rupture planes and their average slips determines that the magnitude of the mainshock is (M_w) 6.92 ± 0.02 . It has substantially increased Coulomb stress (>1.0 bar) on several fault segments near the towns Kuşadası and Söke, and nonnegligibly increased Coulomb stress (>0.1 bar) on several fault segments south of İzmir giving a warning for increased earthquake hazard in this highly inhabited area.

Acknowledgment

We thank The General Directorate of Land Registry and Cadastre, and The General Directorate of Mapping and also Treecomp Company for GPS data. Turkish Office of Navigation, Hydrography and Oceanography is gratefully acknowledged for providing multibeam bathymetry data. Maps and graphs were generated using the GMT and MATLAB. The study was partially supported by the research project "Slip deficit along Major Seismic Gaps in Turkey", which has been funded by Boğaziçi University (project number: 18T03SUP4). We thank Margarita Segou for the discussions on stress change modeling. We appreciate constructive comments by Editor Orhan Tatar, reviewer Şerif Barış and the anonymous reviewer. Science Academy Turkey supported the study through Young Scientist Award (BAGEP), which has been given to Fatih Bulut in 2020.

- Ganas A, Elias P, Briole P, Tsironi V, Valkaniotis S et al. (2020). Fault responsible for Samos earthquake identified. *Temblor*. doi: 10.32858/temblor.134
- Goldstein RM, Werner CL (1998). Radar interferogram filtering for geophysical applications. *Geophysical Research Letters* 25 (21): 4035-4038.
- Gürçay S (2014). Sığacık Körfezi ve çevresinin denizaltı aktif tektoniğinin yüksek çözünürlüklü sismik yöntemler kullanılarak araştırılması. PhD, Dokuz Eylül University, İzmir, Turkey (in Turkish).
- Hager BH, King RW, Murray MH (1991). Measurement of crustal deformation using the Global Positioning System. *Annual Review of Earth and Planetary Sciences* 19 (1): 351-382.
- Kalogeras I, Melis NS, Kalligeris N (2020). The earthquake of October 30th, 2020 at Samos, Eastern Aegean Sea, Greece. *Bruyère-le Châtel, France: The European-Mediterranean Seismological Centre (EMSC)*.
- Kanamori H (1983). Magnitude scale and quantification of earthquakes. *Tectonophysics* 93 (3-4): 185-199.
- King GC, Stein RS, Lin J (1994). Static stress changes and the triggering of earthquakes. *Bulletin of the Seismological Society of America* 84 (3): 935-953.
- Kuşçu İ, Öcal F, Kurtuluş O (2010). İzmir ve Sığacık Körfezleri'nde kıyı ötesi aktif faylar. MTA Rapor No: 11273. Ankara, Turkey: MTA, p. 98 (in Turkish).
- Lienert BR, Havskov J (1995). A computer program for locating earthquakes both locally and globally. *Seismological Research Letters* 66 (5): 26-36.
- Lykousis V, Anagnostou C, Pavlakis P, Rousaki G, Alexandri M (1995). Quaternary sedimentary history and neotectonic evolution of the eastern part of Central Aegean Sea, Greece. *Marine Geology* 128 (1-2): 59-71.
- McClusky S, Balassanian S, Barka A, Demir C, Ergintav S et al. (2000). Global Positioning System constraints on plate kinematics and dynamics in the eastern Mediterranean and Caucasus. *Journal of Geophysical Research: Solid Earth* 105 (B3): 5695-5719.
- Miranda N (2014). Definition of the TOPS SLC deramping function for products generated by the S-1 IPF. European Space Agency Technical Report. Paris, France: European Space Agency.
- Nyst M, Thatcher W (2004). New constraints on the active tectonic deformation of the Aegean. *Journal of Geophysical Research: Solid Earth* 109 (B11).
- Ocakoglu N (2004). İzmir körfezi ve Alaçatı-Doğanbey-Kuşadası açıkları aktif tektoniğinin sismik yansıma verileri ile incelenmesi. PhD, İstanbul Technical University, İstanbul, Turkey.
- Okada Y (1985). Surface deformation due to shear and tensile faults in a half-space. *Bulletin of the Seismological Society of America* 75 (4): 1135-1154.
- Papadimitriou P, Kapetanidis V, Karakonstantis A, Spingos I, Kassaras I et al (2020). First Results on the Mw = 6.9 Samos Earthquake of 30 October 2020. *Bulletin of the Geological Society of Greece* 56 (1): 251-279.
- Reasenber PA, Simpson RW (1992). Response of regional seismicity to the static stress change produced by the Loma Prieta earthquake. *Science* 255 (5052): 1687-1690.
- Saatçılar R, Ergintav S, Demirbaş E, İnan S (1999). Character of active faulting in the North Aegean Sea. *Marine Geology* 160 (3-4): 339-353.
- Sandwell D, Mellors R, Tong X, Xu X, Wei M et al. (2016). GMTSAR: An InSAR Processing System Based on Generic Mapping Tools. 2nd ed. Technical Report. La Jolla, CA, USA: Scripps Institution of Oceanography.
- Sansosti E, Berardino P, Manunta M, Serafino F, Fornaro G (2006). Geometrical SAR image registration. *IEEE Transactions on Geoscience and Remote Sensing* 44: 2861-2870.
- Snoke JA (2003). FOCMEC: focal mechanism determinations. *International Handbook of Earthquake and Engineering Seismology* 85: 1629-1630.
- Sözbilir H, Softa M, Eski S, Tepe Ç, Akgün M, Ankaya Pamukçu O. et al (2020). 30 Ekim 2020 Sisam (Samos) Depremi (Mw: 6,9) Değerlendirme Raporu. DEÜ Deprem Araştırma ve Uygulama Merkezi, 111 s.
- Stiros S, Laborel J, Laborel-Deguen F, Papageorgiou S, Evin et al. (2000). Seismic coastal uplift in a region of subsidence: Holocene raised shorelines of Samos Island, Aegean Sea, Greece. *Marine Geology* 170: 41-58.
- Styron R, Pagani M (2020). The GEM Global Active Faults Database. *Earthquake Spectra* 36(Suppl. 1): 160-180.
- Toda S, Stein RS, Sevilgen V, Lin J (2011). Coulomb 3.3 Graphic-rich deformation and stress-change software for earthquake, tectonic, and volcano research and teaching—user guide. US Geological Survey Open-File Report, 1060, 63. Reston, VA, USA: U.S. Geological Survey.
- Townend J, Zoback MD (2000). How faulting keeps the crust strong. *Geology* 28 (5): 399-402.
- Wang L, Wang R, Roth F, Enescu B, Hainzl S et al. (2009). Afterslip and viscoelastic relaxation following the 1999 M 7.4 Izmit earthquake from GPS measurements. *Geophysical Journal International* 178 (3): 1220-1237.